Xu et al. *NPG Asia Materials* (2019)11:18
https://doi.org/10.1038/s41427-019-0118-x

NPG Asia Materials

ARTICLE Open Access

Ultrathin electronic synapse having high temporal/spatial uniformity and an Al_2O_3/graphene quantum dots/Al_2O_3 sandwich structure for neuromorphic computing

Zhongwei Xu[1], Fushan Li[1], Chaoxing Wu[1,2], Fumin Ma[1], Yueting Zheng[1], Kaiyu Yang[1], Wei Chen[1], Hailong Hu[1], Tailiang Guo[1] and Tae Whan Kim[2]

Abstract

An electronic synapse (e-synapse) based on memristive switching is a promising electronic element that emulates a biological synapse to realize neuromorphic computing. However, the complex resistive switching process it relies on hampers the reproducibility of its performance. Thus, achievement of a reproducible electronic synapse with a high rate of finished products has become a significant challenge in the development of an artificial intelligent circuit. Here, we demonstrate an ultrathin e-synapse having high yield (>95%), minimal performance variation, and extremely low power consumption based on an Al_2O_3/graphene quantum dots/Al_2O_3 sandwich structure that was fabricated using atomic layer deposition. The e-synapse showed both high device-to-device and cycle-to-cycle reproducibility with high stability, endurance, and switching uniformity, because the essential synaptic behaviors could be observed. This implementation of an e-synapse with an Al_2O_3/graphene quantum dots/Al_2O_3 structure should intensify motivation for engineering e-synapses for neuromorphic computing.

Introduction

Differing from computing systems based on the von Neumann architecture, nervous systems of human brain process information based on distributed, parallel, and event-driven computation[1–4]. As a result, biological nervous systems exhibit advantages of fault tolerance and power efficiency for real-world problems involving visual information, audio recognition, and movement control. The idea of building an electronic system that can mimic part of the function of a biological nervous system is currently attracting significant interest[5]. However, as many as 10^{14} synapses are present in the human cerebral cortex, making hardware implementation with massively parallel and compact electronic systems exceptionally challenging due to the lack of a compact electronic element[6,7].

Two-terminal memristive devices are promising candidates to act as a compact electronic element and have been widely demonstrated in the pursuit of certain synaptic functions[8–10]. Specifically, synaptic operations, including long-term potentiation/depression (LTP/LTD), short-term potentiation/depression (STP/STD), spike-timing-dependent plasticity (STDP) learning rules, paired-pulse facilitation (PPF), and low-power consumption have been extensively simulated in these electronic synapses (e-synapses)[11–28]. However, e-synapses usually suffer from unavoidable temporal (cycle-to-cycle) and spatial (device-to-device) variations due to their intrinsic working mechanism and structure interaction. These variations exist because most two-terminal e-synapses

Correspondence: Fushan Li (fsli@fzu.edu.cn) or Chaoxing Wu (chaoxing_wu@hotmail.com) or Tae Whan Kim (twk@hanyang.ac.kr)
[1]Institute of Optoelectronic Technology, Fuzhou University, 350116 Fuzhou, China
[2]Department of Electronic and Computer Engineering, Hanyang University, Seoul 133-791, Republic of Korea

operate by relying on conducting filamentary switching behaviors, random carrier capture and release, or electrode–dielectric interface modulation. Thus, the intrinsic uncontrollable filament dynamics in the active dielectric or the uncontrollable carrier transport through the disordered traps in a hybrid layer lead to performance vibrations and device malfunctions[29]. The low yield and the unavoidable temporal/spatial variations make large-scale artificial intelligence chips for analog neural computing impractical. As a result, the achievement of a stable e-synapse with high yield and reproducibly becomes an essential step.

Here, we demonstrate an ultrathin (<10 nm) e-synapse with high performance reproducibility, high yield (>95%), and low power consumption. The e-synapses show both high device-to-device and cycle-to-cycle reproducibility with high stability, endurance, and switching uniformity. These performances are achieved through the two-dimensional confinement of graphene quantum dots (GQDs) in ultrathin Al_2O_3 layers to form a sandwich structure. Differing from conducting filamentary-based switching behaviors, the operation of our e-synapse is based on quantum tunneling; that is, a small number of electrons manage to jump through the ultrathin Al_2O_3/GQDs/Al_2O_3 structure. Thus, only the thickness of the Al_2O_3/GQDs/Al_2O_3 structure has a dominant effect on the electron transport in the e-synapse. Due to the exactly controllable thickness and the high reproducibility of the Al_2O_3/GQDs/Al_2O_3 stacking layer fabricated using atomic layer deposition (ALD), the e-synapses exhibit high temporal (cycle-to-cycle) and spatial (device-to-device) uniformity. Furthermore, the low tunneling currents lead to ultralow power consumption. Based on the electrical performance, the essential functions of a single artificial synapse, such as synaptic plasticity, STD, LTP, and PPF, are observed in our fabricated e-synapses. The implementation of the Al_2O_3/GQDs/Al_2O_3 stacking layer provides a new perspective for engineering a large-scale, neuromorphic computing system.

Materials and methods

Fabrication of e-synapses

ITO-coated glass substrates were cleaned ultrasonically in acetone and ethanol for 20 min each. After the substrates had been chemically cleaned, they were annealed in a vacuum oven for 30 min at 90 °C. Then, an ultrathin Al_2O_3 film was deposited on the ITO-coated glass using ALD (beneq TFS 200) at 90 °C with trimethylaluminum (TMA) and water as precursors. The carrier gas in the viscous flow reactor was N_2. The pressure of the N_2 carrier gas was <0.1 MPa. TMA and H_2O were alternately entrained in the N_2 carrier flow to produce linear-controlled and atomic-layer-controlled Al_2O_3 growth. The as-synthesized Al_2O_3 film was treated with ultraviolet ozone (UVO, BZS250GF-TC) for 20 min to increase its surface hydrophilicity. For the preparation of the GQDs layer, a GQD aqueous solution (1 mg/ml, CAS:7440-44-0, Nanjing XFNANO Materials TECH Co., Ltd) was spin-coated onto the Al_2O_3 film at 500 rpm for 5 s and 2000 rpm for 50 s, followed by annealing at 90 °C for 20 min. Another ultrathin Al_2O_3 film was deposited on the Al_2O_3/GQDs stacking layers using ALD. Finally, the top Ag electrodes, each with a thickness of 100 nm and a diameter of 1 mm, were deposited on the Al_2O_3/GQDs/Al_2O_3 layer using thermal evaporation through a metal mask at a system pressure of 5×10^{-4} Pa.

Characterization and output measurement

Atomic force microscope (AFM; Bruker multimode 8), transmission electron microscopy (TEM; FEI Titan ETEM G2), ultraviolet photoelectron spectroscopy (UPS; ESCALAB 250) were used to characterize the GQDs. A Keithley 4200 semiconductor characterization system was utilized to measure the electrical output of the devices. All electrical measurements were carried out at room temperature under atmospheric pressure.

Results and discussion

Device structure

Al_2O_3 is known to be a well-behaved system that can be fabricated using ALD with a variety of precursors and with relatively short cycle times[30]. Thus, the thickness of the Al_2O_3 layer can be accurately controlled when ALD is used for fabrication. The fabrication procedure for the e-synapses based on the ultrathin Al_2O_3/GQDs/Al_2O_3 sandwich structure is presented in Fig. 1a. The ultrathin Al_2O_3 film was first deposited on indium tin oxide (ITO)-coated glass using ALD. Then, the GQDs were deposited on the surface of the Al_2O_3 using spin coating. Another ultrathin Al_2O_3 film was deposited to form the Al_2O_3/GQDs/Al_2O_3 sandwich structure. As shown in the AFM images of the Al_2O_3/GQDs stacking layer (Fig. 1b), GQDs with a thickness of ~1.4 nm were dispersed on the Al_2O_3 film. Because of the high hydrophilicity of the Al_2O_3 film, the GQDs can be easily spin-coated onto the surface of the Al_2O_3 film. Both the accurately controlled thickness of the Al_2O_3 film, which is due to the use of ALD, and the well-dispersed GQDs contribute to the high yield and high device-to-device uniformity of our e-synapses, which will be discussed later.

The charge-trapping processes can be engineered by reducing the size of the particles to the nanometer scale. The GQD with a lateral size of ~15 nm (Fig. 1c) is the key component of our e-synapse. The UV photoemission spectroscopy (UPS) spectra show that the highest occupied molecular orbital (HOMO) and the lowest unoccupied molecular orbital (LUMO) of the GQDs were −5.9 and −4.0 eV, respectively (Fig. 1d). As a result, the

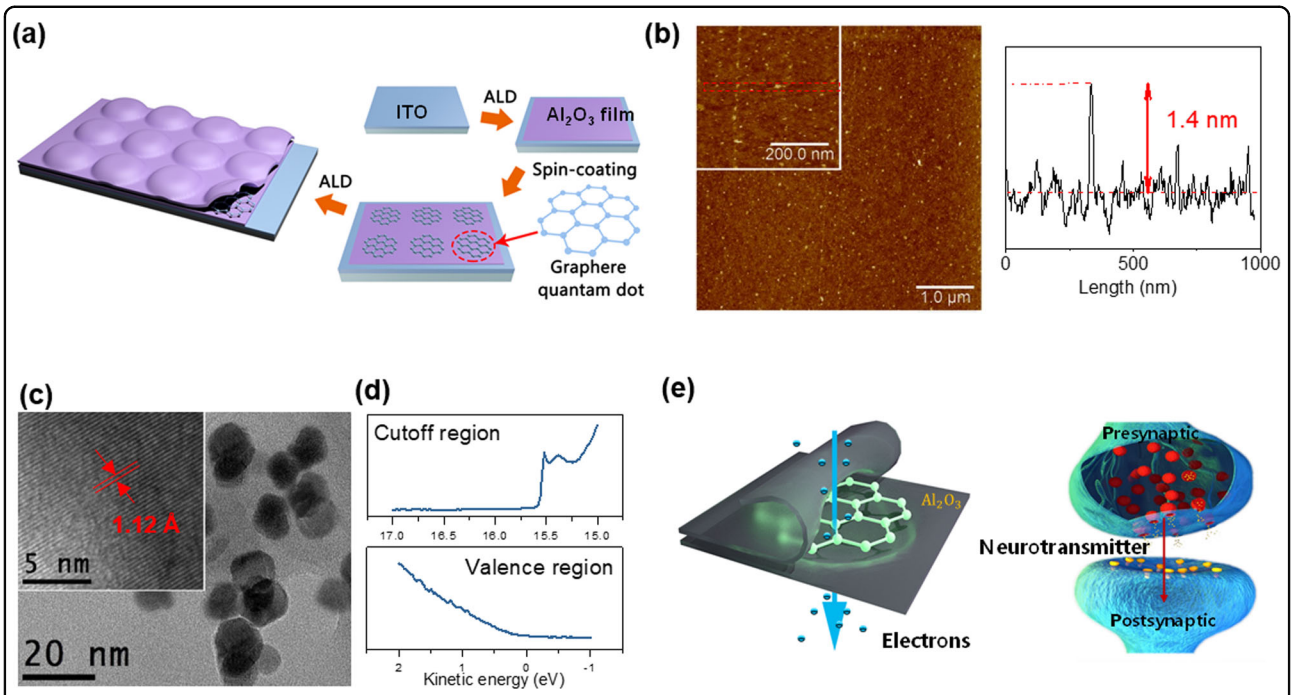

Fig. 1 Structure and design. a Schematic of the fabrication procedure for the e-synapse with the Al_2O_3/GQDs/Al_2O_3 configuration. **b** AFM image of the GQDs deposited on Al_2O_3 and the section height profile. The inset presents a high-magnification AFM image. **c** TEM images of the GQDs. The inset presents a high-magnification image. **d** UPS spectra of the GQDs: cutoff region (top) and valence region (bottom). **e** The commonality between the e-synapse and the biological chemical synapse

two-dimensionally confined GQDs wrapped by ultrathin Al_2O_3 films (Fig. 1e) acted as electron traps to modulate the Fowler–Nordheim tunneling-based electron transport. The overall effect is that the conductance of the Al_2O_3/GQDs/Al_2O_3 layer is tunable, which is similar to synaptic plasticity in biological nervous systems (Fig. 1e).

Electrical properties and working mechanisms

Our e-synapse is equivalent to the parallel combination of a memristor with a capacitor (Fig. 2a). Notably, the thickness of the Al_2O_3 film has a remarkable influence on the device performance under a direct-current (DC) voltage sweep. The measured current decreases with increasing Al_2O_3 film thickness (Figs. S1–S4). Typical electrical performances of an optimized e-synapse with a structure of Al_2O_3 (4 nm)/GQD/Al_2O_3 (4 nm) under consecutive positive and negative DC voltage sweeps are shown in Fig. 2b and c, respectively. The voltage was applied to the ITO bottom electrode while the Ag top electrode was electrically grounded. In this case, the e-synapse dominantly acts like a memristor. In contrast to the bistable/multilevel resistive switching for digital memory applications[31], the electrical performances of our e-synapse demonstrate a smoother tuning of the conductance during the voltage sweeping processes. When 15 consecutive sweeps of positive DC voltages (0–3 V) were applied, the current level continuously decreases with an increasing number of sweeps (Fig. 2b). In other words, the e-synapse shows a gradual transition from a low-resistance state (LRS) to a high-resistance state (HRS) and finally reaches a saturation state. The gradual variation in the conductance with increasing number of applied voltage sweeps is similar to a variable synaptic weight, that is, a variable connection strength[32]. It is worth noting that a similar phenomenon also exists after inverting the polarity of the voltage. While the e-synapse remains in the HRS, additional consecutive DV voltage sweeps with a negative polarity were applied, and the conductance also decreased with increasing number of sweeps, as shown in Fig. 2c. Because a larger voltage (>2 V) with negative polarity would result in device breakdown, negative DC voltage sweeps with lower amplitudes (0 to −2 V) were applied in this measurement, as shown in Fig. 2c.

The conductance of the Al_2O_3/GQD/Al_2O_3 layer can also be modulated by continually applying voltage pulses. As shown in the left panel of Fig. 2d, when 20 consecutive positive pulses with an amplitude of 1.2 V, a duration of 0.1 s, and a period of 0.4 s (2.5 Hz) were applied to modulate the conductance of the device, the recorded current gradually decreased with an increasing number of consecutive positive pulses and finally reached a minimum current saturation. However, the first negative pulse (−1.2 V, 0.1 s, 2.5 Hz) switched the device to low current

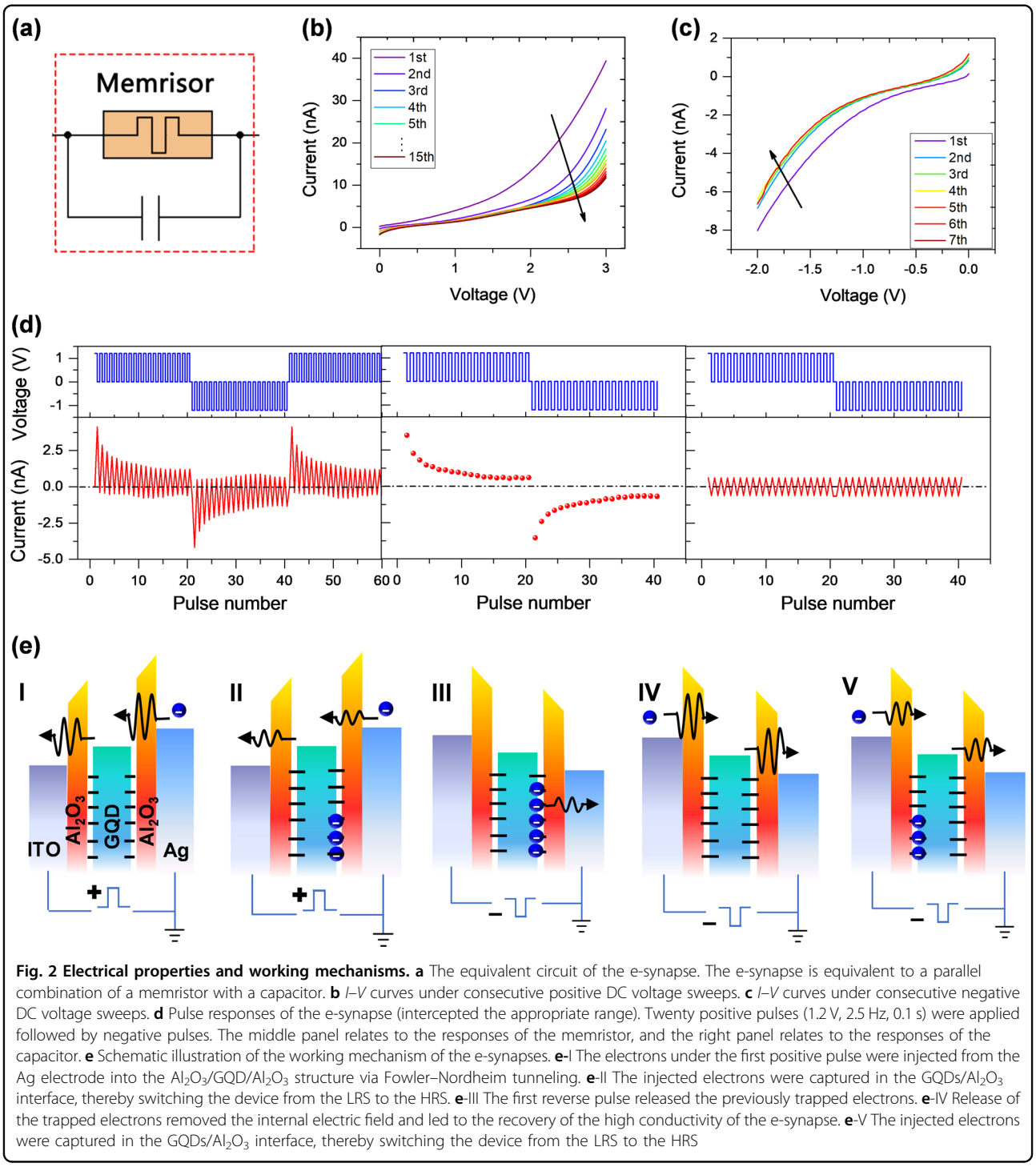

Fig. 2 Electrical properties and working mechanisms. a The equivalent circuit of the e-synapse. The e-synapse is equivalent to a parallel combination of a memristor with a capacitor. **b** *I–V* curves under consecutive positive DC voltage sweeps. **c** *I–V* curves under consecutive negative DC voltage sweeps. **d** Pulse responses of the e-synapse (intercepted the appropriate range). Twenty positive pulses (1.2 V, 2.5 Hz, 0.1 s) were applied followed by negative pulses. The middle panel relates to the responses of the memristor, and the right panel relates to the responses of the capacitor. **e** Schematic illustration of the working mechanism of the e-synapses. **e**-I The electrons under the first positive pulse were injected from the Ag electrode into the Al_2O_3/GQD/Al_2O_3 structure via Fowler–Nordheim tunneling. **e**-II The injected electrons were captured in the GQDs/Al_2O_3 interface, thereby switching the device from the LRS to the HRS. **e**-III The first reverse pulse released the previously trapped electrons. **e**-IV Release of the trapped electrons removed the internal electric field and led to the recovery of the high conductivity of the e-synapse. **e**-V The injected electrons were captured in the GQDs/Al_2O_3 interface, thereby switching the device from the LRS to the HRS

level again. The following 19 consecutive negative pulses could have also depressed the conductance. The amplitudes of the currents measured under pulse stimulations were consistent with those measured under DC voltage sweep stimulations, as shown in Fig. S5. Interestingly, after the application of a sufficient number of negative pulses, the e-synapse returned to its original high conductance state measured under positive pulses. Thus, the application of negative biases was actually a potentiation process in which the conductance increases if measured under a positive bias. Note that the initial positive (negative) current may have been modulated due to the previously applied negative (positive) pulses, which will be discussed later.

Our e-synapse has a metal–insulator–metal structure with the ultrathin Al_2O_3/GQD/Al_2O_3 structure sandwiched between two electrodes. Thus, the device also behaves as a capacitor (Fig. S6). The e-synapse exhibits obvious capacitance characteristics under pulse stimulation. When a positive pulse is applied to the device, the capacitor is charged. Thus, a positive current can be recorded. When the positive pulse is removed, a negative current can be recorded. The negative current is related to the discharge current from the capacitor. The positive current consists of two components: the tunneling current related to the response of the memristor and the charging current related to the charging response of the capacitor (Fig. S7). Considering the approximation that the value of the charging current is the same as that of the discharging current, we can extract the response of the memristor by subtracting the capacitance signal from the original signal. As a result, the current response of the e-synapse under pulse stimulation can be divided into two components: the response of the capacitor (the right panel of Fig. 2d) and the response of the memristor (the middle panel of Fig. 2d). The conductivity of the memristor decreased continuously from 2.9 to 0.7 nS under 20 consecutive positive pulses.

The gradual variation of the conductance was attributed to the introduction of the GQDs (Fig. S8). GQDs are known to have superior properties of variations in the energy levels and a large specific surface area for potential applications in electronics[33]. The charge-storage ability derived from the GQDs can affect the carrier transport. The operating mechanism of the e-synapse can be illustrated by using schematic diagrams of the energy bands, as shown in Fig. 2e. The electrons under the first positive pulse are injected from the Ag electrode into the Al_2O_3/GQD/Al_2O_3 structure via Fowler–Nordheim tunneling (Fig. 2e-I). In that case, the current is the highest. However, some of the injected electrons are captured in the GQDs/Al_2O_3 interface, resulting in the formation of negative space charges (Fig. 2e-II). These negative space charges can induce an internal electric field pointing to the negative charges. As a result, the external electric field between the GQDs and the Ag electrode is weakened, so the electron injection from the Ag electrode into the Al_2O_3/GQD/Al_2O_3 structure is inhibited. Thus, the conductivity of the e-synapse decreases, and the e-synapse tends to switch from the LRS to the HRS. The first reverse pulse can release the previously trapped electrons (Fig. 2e-III), which removes the internal electric field, thereby allowing the conductivity to recover (Fig. 2e-IV). As a result, the first negative pulse switches the device to the high-current state again. However, the electrons that are injected under the following reverse-polarity pulses are captured by the GQDs/Al_2O_3 interface, resulting in a switch from the LRS to the HRS (Fig. 2e-V). When the polarity of the pulse reverses again, the above process is repeated. As a result, the e-synapse is expected to exhibit high operation stability.

Temporal and spatial uniformity

The temporal variation of an e-synapse under 12,000 pulses was characterized by applying a sequence of electric pulses, and the results are shown in Fig. 3a. The e-synapse showed high operation endurance and cycle-to-cycle reproducibility. Furthermore, our e-synapse showed high stability even under atmospheric conditions. The performance of the fresh device (Fig. 3b) was almost the same as that of the device that had been placed in the atmosphere for 100 days (Fig. 3c). This cycle-to-cycle uniformity and high stability of our e-synapse are in sharp contrast to those of many devices operating based on conducting filamentary switching behaviors, random carrier capture-release, or electrode–dielectric interface modulation[29]. In traditional research, the intrinsic uncontrollable filament dynamics in an active dielectric or the uncontrollable carrier transport through the disordered traps in the hybrid layer can lead to variations in the device's performance and to device malfunction. However, the carrier transport of our e-synapse is controllable. The GQDs, which act as electron traps, are uniformly and two dimensionally confined in the ultrathin Al_2O_3 layer and modulate the Fowler–Nordheim tunneling-based carrier transport process, which contributes to the low temporal variation.

In addition to the temporal uniformity, our e-synapses also exhibit excellent spatial uniformity with a device yield >95%. As shown in Fig. 3d, 20 consecutive positive pulses and then 20 consecutive negative pulses were applied to modulate the conductance of 150 e-synapses. All measured e-synapses showed comparable switching behaviors and uniform device-to-device performances. The distributions of the LRS and the HRS for the measured 150 e-synapses show little variation, as shown in Fig. 3e. The measured conductance under the first ±1.2-V pulse is defined as the conductance of the LRS while the measured conductance under the last ±1.2-V pulse is defined as the conductance of the LRS. The high device yield and device-to-device uniformity are attributed to the ability to accurately control the thickness of the Al_2O_3 film when the film is deposited using ALD and to the uniform distribution of GQDs on the surface of the Al_2O_3.

Synaptic STD, LTP, and PPF

Synaptic plasticity in neuromorphic systems is regarded as a basic function for learning and memory. Specifically, the potentiation and depression of a biological synapse are usually achieved through action potential spikes. Figure 4a shows the results of our e-synapse programmed using a series of 20 identical positive pulses (1.2 V, 0.1 s). The

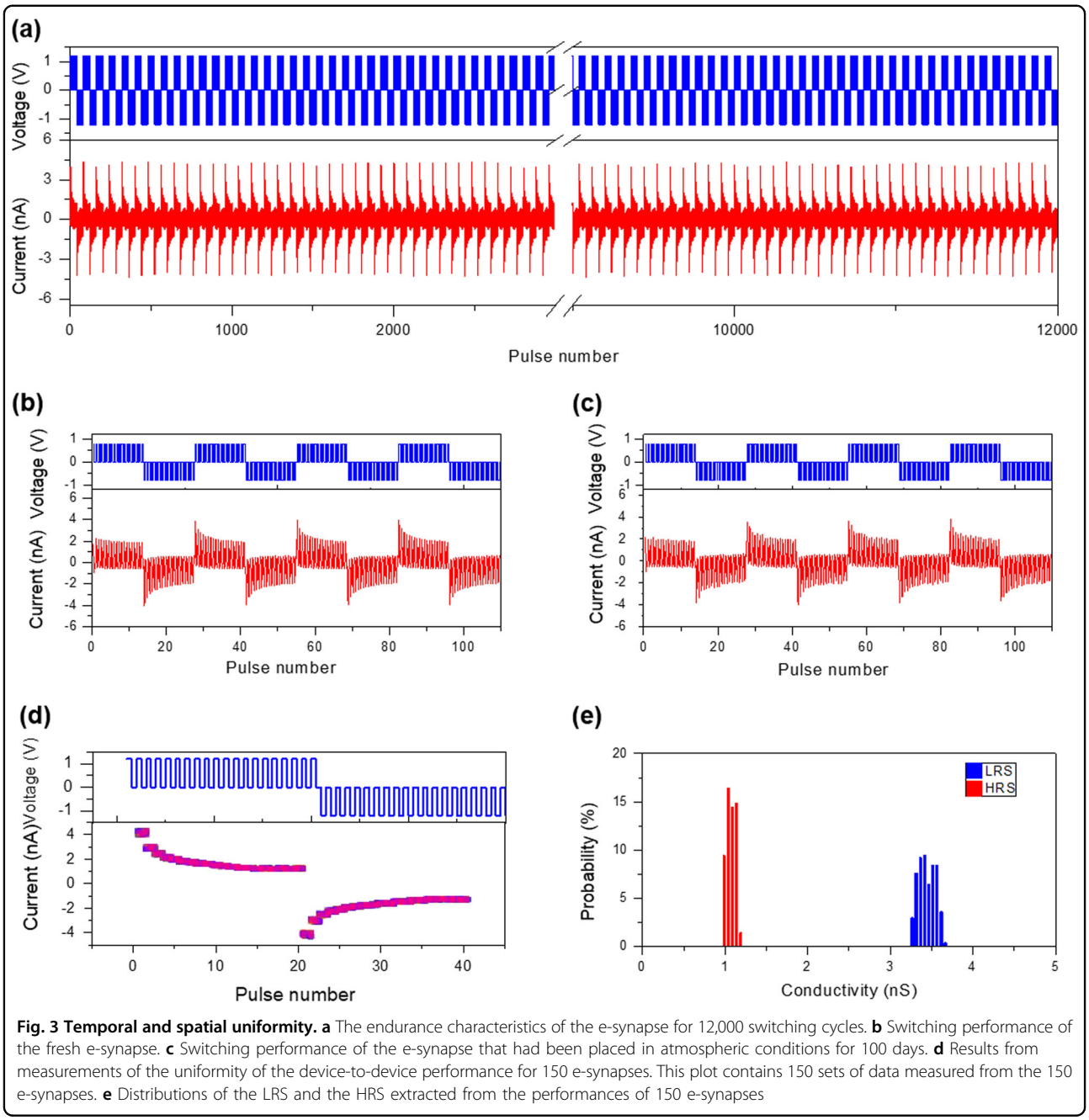

Fig. 3 Temporal and spatial uniformity. a The endurance characteristics of the e-synapse for 12,000 switching cycles. **b** Switching performance of the fresh e-synapse. **c** Switching performance of the e-synapse that had been placed in atmospheric conditions for 100 days. **d** Results from measurements of the uniformity of the device-to-device performance for 150 e-synapses. This plot contains 150 sets of data measured from the 150 e-synapses. **e** Distributions of the LRS and the HRS extracted from the performances of 150 e-synapses

conductance (G), namely, the synaptic weight, gradually decreases with an increasing number of positive pulses, and this characteristic is related to the synaptic depression process. Interestingly, the variation in the conductance (ΔG) produced by a pulse depends on the previous conductance[6]. The relation between ΔG and G is presented in Fig. 4b. Based on ΔG or G, we can mine historical information of the voltage applied to the e-synapse. Additionally, the number of positive pulses applied to the e-synapse can be approximately calculated based on the measured values of ΔG and G, as shown in Fig. 4c. For example, for $G = 3$ nS, the total number of effective pulses is one whereas the total number of effective pulses is 3 for $\Delta G = 0.3$ nS. This potentially represents the function of recovering information about the memory system.

Typically, memory in the human brain is temporary. The transient memory or short-term memory, which only lasts for seconds or minutes, can be easily interrupted by accidental electrical shock and can decay rapidly. We also investigated the memory retention of our e-synapses. The e-synapse was set to the HRS by applying a sufficient number of positive pulses; then, the conductivity of the

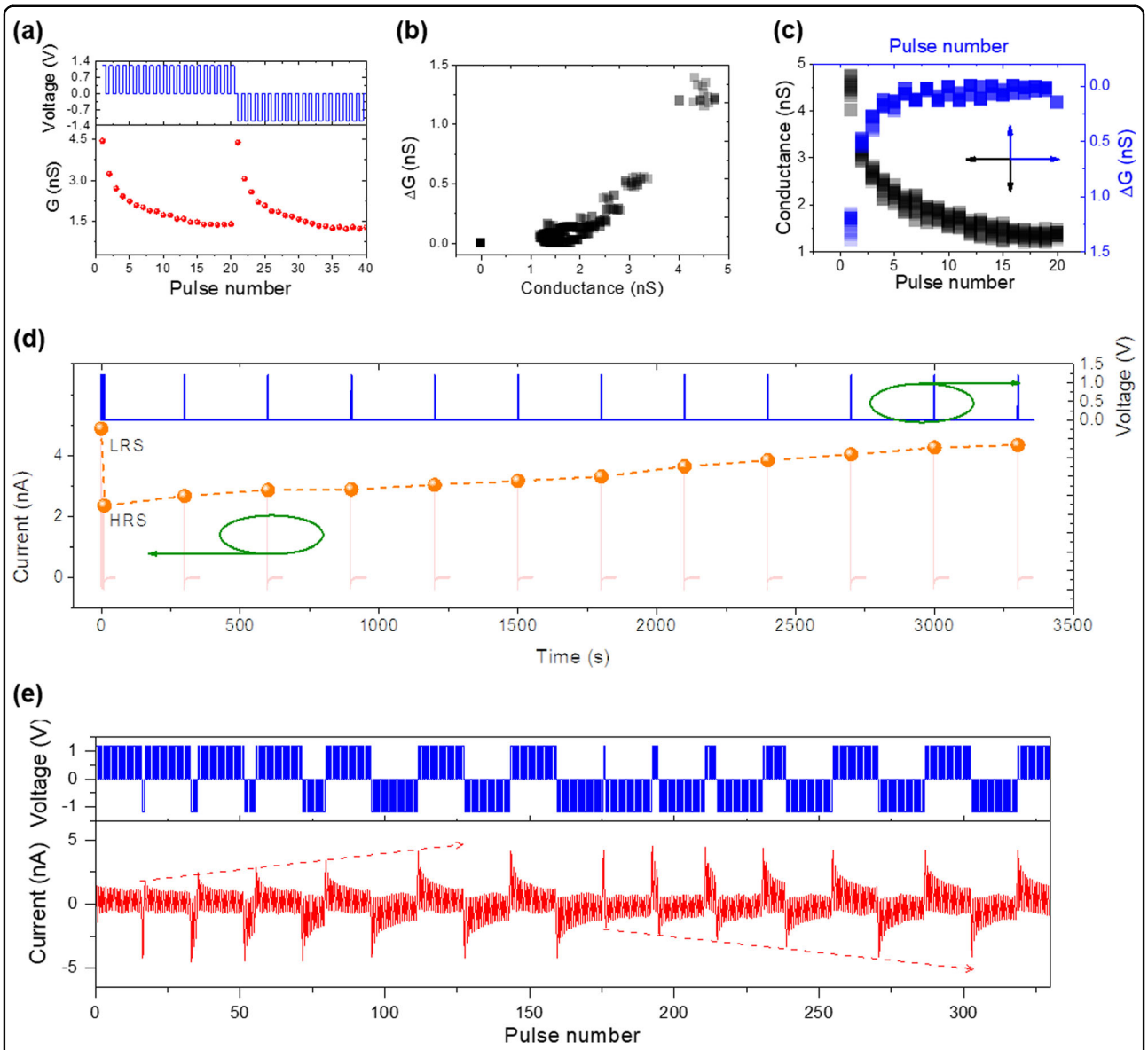

Fig. 4 Synaptic plasticity performances. a Switching behaviors under a sequence of positive pulses. The positive pulse can decrease the conductance *G* of the e-synapse, resulting in synaptic depression. **b** Conductance variation Δ*G* as a function of the initial conductance. **c** *G* and of Δ*G* as a function of the pulse number. **d** Results of the memory retention measurement. The e-synapse is set to the HRS by applying a sufficient number of positive pulses; then, the e-synaptic conductance is read by applying a 1.2-V pulse every 5 min. **e** Results from the synaptic potentiation measurement. In this measurement, 20 identical positive pulses (1.2 V, 0.1 s, 2.5 Hz) followed by 1, 3, 5, 10, and 20 negative pulses, respectively, were applied. Subsequently, 20 identical negative pulses (1.2 V, 0.1 s, 2.5 Hz) followed by 1, 3, 5, 10, and 20 positive pulses, respectively, were applied

e-synapse was measured by applying a 1.2-V pulse every 5 min. As shown in Fig. 4d, the recorded current gradually increased over time, representing a slow transition from an HRS to an LRS. After ~1 h, the e-synapse recovered to the LRS. This phenomenon is similar to the behavior of forgetting in the human brain. As a result, the switching process from the LRS to the HRS under positive bias stimulation is equivalent to the process of short-term depression (STD). The mechanism for this phenomenon is the spontaneous release of captured electrons.

The energy consumption for one operation can be calculated by multiplying the pulse's amplitude by the current flowing across the device at each point in time ($E = V \times I \times t$) and taking an integral over the operating time. In this work, the highest current in the high-conductance state is <5 nA; thus, low-energy consumption is achieved. A greater resistance of the initial state results in the device consuming lower energy per pulse. The energy consumption for the first pulse stimulation in the depression process was ~0.48 nJ/spike.

The energy consumption also decreased with an increasing number of pulse stimulations. The energy consumption in the HRS was <0.16 nJ/spike due to the low operating current.

As mentioned above, the e-synapse in the HRS can return to its original high conductance state after the application of negative pulses. Here, we investigate the synaptic potentiation in detail. We assume that the e-synapse normally operates under positive bias. We applied 20 identical positive pulses (1.2 V, 0.1 s, 2.5 Hz) followed by 1, 4, 5, 10, and 20 negative pulses. As shown in Fig. 4e, each negative pulse tended to increase the conductivity of the e-synapse measured under positive bias. After the application of a sufficient number of negative pulses (>10), the e-synapse was able to completely return to its original high conductance state measured under positive pulses. Conversely, each positive pulse tended to increase the conductivity under negative bias. Thus, the application of a reverse bias is actually a potentiation process. Furthermore, when the fact that the e-synapse that is initially in the LRS is considered, the switching process from the HRS to the LRS under negative bias stimulation was the process of LTP.

Presynaptic spikes are well known to be able to trigger a postsynaptic current through synapses in a postsynaptic neuron to establish dynamic logic in a neural network[34]. Among the basic dynamic logic functions, PPF is an important short-term phenomenon. PPF states that when two presynaptic spikes are applied successively, the second spike will generate a more remarkable output than the first pulse[35]. Additionally, the amplitude of the output caused by the second pulse is determined by the time interval between the two pulses, and a larger interval might lead to a smaller amplitude change. PPF was demonstrated in our e-synapse by applying positive pulses with different amplitudes and frequencies. As shown in Fig. 5a, a series of positive pulses with amplitude of 0.2 V and duration of 0.1 s were first applied. Similar to PPF studies in biology, the intervals between pulses (frequencies) were changed systemically to probe the responses. As shown in the left panel of Fig. 5a, a pulse with amplitude of 0.2 V (0.5 Hz) was too low to change the conductance of the e-synapse. However, when the frequency of the pulse was increased (0.8 Hz), the interval between the pulses decreased, and the conductance measured during the second pulse was indeed less than that measured during the first pulse, similar to a PPF effect (middle panel of Fig. 5a). The conductance of the e-synapse decreased when stimulated by a series of pulses, which represents a slow switching from an LRS to an HRS. As the stimulation frequency increased (1.25 Hz), the decrease in conductance was more significant, as shown in the right panel of Fig. 5a. When 1.2-V pulse trains with low frequency (0.5 Hz) were used to stimulate the e-synapses, the stimulation was strong enough to depress the conductivity (left panel of Fig. 5a). However, a similar PPF phenomenon was also observed. The decrease in the conductance became faster with an increase in the

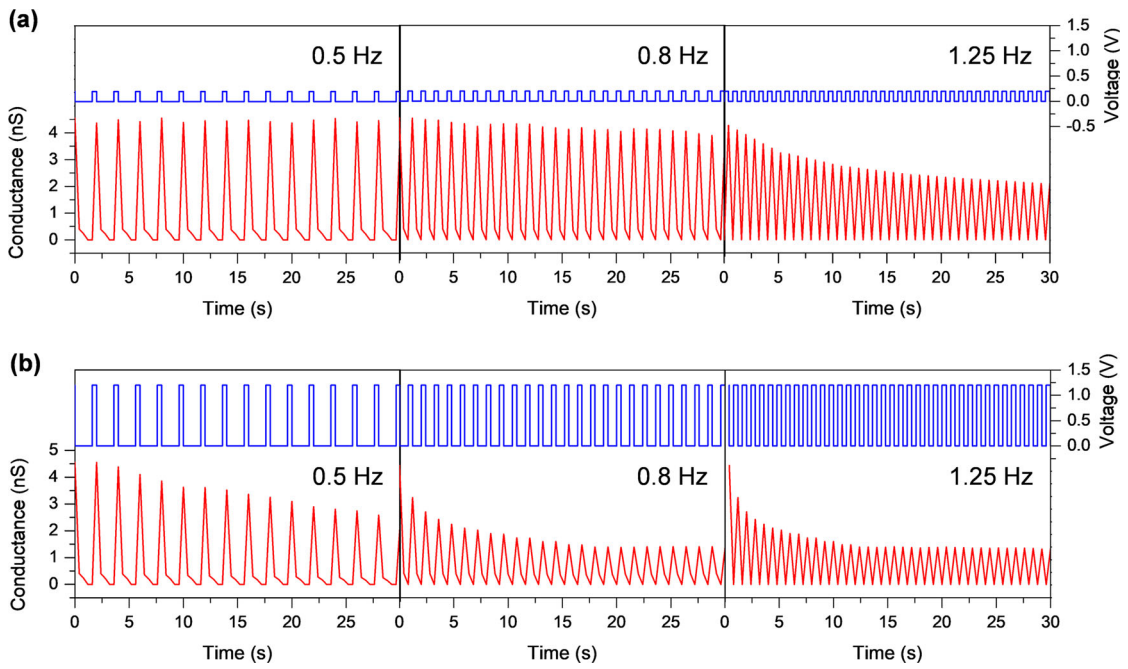

Fig. 5 PPF characteristics and responses at different voltages and frequencies. The e-synapse was stimulated by (**a**) a 0.2-V pulse at 0.5, 0.8, and 1.25 Hz, respectively, and by (**b**) a 1.2-V pulse at 0.5, 0.8, and 1.25 Hz, respectively

stimulation frequency, as shown in the middle and right panels of Fig. 5b. The results indicate that the stimulation frequency will affect the memory function of the e-synapses. Even though the input is not strong enough to excite memory, high-frequency stimulation can excite the e-synapse. In other words, our e-synapse tends to remember high-frequency input events. This frequency dependence can be explained using the electron capture process in the GQDs. Under an external electric field, the injected electrons will be captured in the GQDs. However, the captured electrons can be released spontaneously. Pulse trains with a higher frequency will reduce the number of released electrons and result in a more effective accumulation of captured electrons in the GQDs.

Conclusions

In summary, we demonstrated an ultrathin e-synapse that had a high yield (>95%), a high performance uniformity, and low power consumption and that functioned primarily on the basis of controllable Fowler–Nordheim tunneling. The high device yield, device-to-device uniformity, and cycle-to-cycle uniformity are attributed to the ability to accurately control the thickness of the Al_2O_3 film when it is deposited using ALD and to the uniform distribution of GQDs on the surface of the Al_2O_3 film. The ability of GQDs to capture/release electrons functionally leads to gradual changes in conductance that emulate the essential synaptic functions of LTP, STD, and PPF. Our research presents methods that use GQDs together with ALD to develop highly reproducible artificial synapses; such synapses should provide a new perspective on and increase the motivation for engineering e-synapses for neuromorphic computing.

Acknowledgements

This work was supported by the National Key Research and Development Program of China (2016YFB0401305), the National Natural Science Foundation of China (U1605244), the Natural Science Foundation of Fujian Province (2016J01296), and the National Research Foundation of Korea (NRF) funded by the Ministry of Education, Science and Technology (2016R1A2A1A05005502).

Conflict of interest

The authors declare that they have no conflict of interest.

Supplementary information is available for this paper at https://doi.org/10.1038/s41427-019-0118-x.

Received: 17 October 2018 Revised: 27 December 2018 Accepted: 27 January 2019
Published online: 19 April 2019

References

1. Von Neumann, J. *The Computer and the Brain* (Yale University Press, New Haven, Connecticut, United States, 2012). ISBN 9780300181111.
2. Krogh, A. What are artificial neural networks? *Nat. Biotechnol.* **26**, 195 (2008).
3. Wu, C. et al. Mimicking classical conditioning based on a single flexible memristor. *Adv. Mater.* **29**, 1602890 (2017).
4. Furber, S. Large-scale neuromorphic computing systems. *Neural Eng.* **13**, 051001 (2016).
5. Perea, G., Navarrete, M. & Araque, A. Tripartite synapses: astrocytes process and control synaptic information. *Trends Neurosci.* **32**, 421–431 (2009).
6. Wu, C., Kim, T. W., Choi, H. Y., Strukov, D. B. & Yang, J. J. Flexible three-dimensional artificial synapse networks with correlated learning and trainable memory capability. *Nat. Commun.* **8**, 752 (2017).
7. Kuzum, D., Yu, S. & Wong, H. S. Synaptic electronics: materials, devices and applications. *Nanotechnology* **24**, 382001 (2013).
8. Prezioso, M. et al. Training and operation of an integrated neuromorphic network based on metal-oxide memristors. *Nature* **521**, 61–64 (2015).
9. Yang, J. J., Strukov, D. B. & Stewart, D. R. Memristive devices for computing. *Nat. Nanotechnol.* **8**, 13–24 (2013).
10. Lee, H. E. et al. Novel electronics for flexible and neuromorphic computing. *Adv. Funct. Mater.* **28**, 1801690 (2018).
11. Li, B. et al. Mediating short-term plasticity in an artificial memristive synapse by the orientation of silica mesopores. *Adv. Mater.* **30**, 1706395 (2018).
12. Tu, L. et al. A wide-range operating synaptic device based on organic ferroelectricity with low energy consumption. *RSC Adv.* **8**, 26549–26553 (2018).
13. Lee, T. H. et al. Synaptic plasticity and metaplasticity of biological synapse realized in a $KNbO_3$ memristor for application to artificial synapse. *ACS Appl. Mater. Interfaces* **10**, 25673–25682 (2018).
14. Liu, G. et al. Organic biomimicking memristor for information storage and processing applications. *Adv. Electron. Mater.* **2**, 1500298 (2016).
15. Yang, K. et al. Tunable flexible artificial synapses: a new path toward a wearable electronic system. *npj Flex. Electron.* **2**, 20 (2018).
16. John, R. A. et al. Synergistic gating of electro-iono-photoactive 2D chalcogenide neuristors: coexistence of hebbian and homeostatic synaptic metaplasticity . *Adv. Mater.* **30**, 1800220 (2018).
17. Park, Y. & Lee, J. S. Artificial synapses with short- and long-term memory for spiking neural networks based on renewable materials. *ACS Nano* **11**, 8962–8969 (2017).
18. Du, C., Ma, W., Chang, T., Sheridan, P. & Lu, W. D. Biorealistic implementation of synaptic functions with oxide memristors through internal ionic dynamics. *Adv. Funct. Mater.* **25**, 4290–4299 (2015).
19. Kim, S. et al. Experimental demonstration of a second-order memristor and its ability to biorealistically implement synaptic plasticity. *Nano Lett.* **15**, 2203–2211 (2015).
20. Yang, C.-S. et al. Electrochemical-reaction-induced synaptic plasticity in MoO x-based solid state electrochemical cells. *Phys. Chem. Chem. Phys.* **19**, 4190–4198 (2017).
21. Wang, Z. et al. Memristors with diffusive dynamics as synaptic emulators for neuromorphic computing. *Nat. Mater.* **16**, 101 (2017).
22. Xu, W. et al. Organometal halide perovskite artificial synapses. *Adv. Mater.* **28**, 5916–5922 (2016).
23. Wang, L. et al. Rectification-regulated memristive characteristics in electron-type CuPc-based element for electrical synapse. *Adv. Electron. Mater.* **3**, 1700063 (2017).
24. Wang, C., He, W., Tong, Y. & Zhao, R. Investigation and manipulation of different analog behaviors of memristor as electronic synapse for neuromorphic applications. *Sci. Rep.* **6**, 22970 (2016).
25. Li, Y. et al. Ultrafast synaptic events in a chalcogenide memristor. *Sci. Rep.* **3**, 1619 (2013).
26. Wang, Z. Q. et al. Synaptic learning and memory functions achieved using oxygen ion migration/diffusion in an amorphous InGaZnO memristor. *Adv. Funct. Mater.* **22**, 2759–2765 (2012).
27. Ohno, T. et al. Short-term plasticity and long-term potentiation mimicked in single inorganic synapses. *Nat. Mater.* **10**, 591–595 (2011).
28. Chang, T., Jo, S. H. & Lu, W. Short-term memory to long-term memory transition in a nanoscale memristor. *ACS Nano* **5**, 7669–7676 (2011).
29. Choi, S. et al. SiGe epitaxial memory for neuromorphic computing with reproducible high performance based on engineered dislocations. *Nat. Mater.* **17**, 335–340 (2018).

30. Groner, M., Fabreguette, F., Elam, J. & George, S. Low-temperature Al_2O_3 atomic layer deposition. *Chem. Mater.* **16**, 639–645 (2004).
31. Wu, C., Li, F. & Guo, T. Efficient tristable resistive memory based on single layer graphene/insulating polymer multi-stacking layer. *Appl. Phys. Lett.* **104**, 183105 (2014).
32. Iyer, R., Menon, V., Buice, M., Koch, C. & Mihalas, S. The influence of synaptic weight distribution on neuronal population dynamics. *PLoS Comput. Biol.* **9**, e1003248 (2013).
33. Choi, H. Y., Wu, C., Bok, C. H. & Kim, T. W. Organic electronic synapses with pinched hystereses based on graphene quantum-dot nanocomposites. *NPG Asia Mater.* **9**, e413 (2017).
34. Cash, S. & Yuste, R. Linear summation of excitatory inputs by CA1 pyramidal neurons. *Neuron* **22**, 383–394 (1999).
35. Zucker, R. S. & Regehr, W. G. Short-term synaptic plasticity. *Annu. Rev. Physiol.* **64**, 355–405 (2002).